A new view on abrupt climate changes and the bipolar seesaw based on paleotemperatures from Iberian Margin sediments

Nina Davtian, Edouard Bard

PNAS RESEARCH ARTICLE | EARTH, ATMOSPHERIC, AND PLANETARY SCIENCES OPEN ACCESS

A new view on abrupt climate changes and the bipolar seesaw based on paleotemperatures from Iberian Margin sediments

Nina Davtian[a,1,2] and Edouard Bard[a,2]

Contributed by Edouard Bard; received June 2, 2022; accepted February 2, 2023; reviewed by Jerry F. McManus, Eelco J. Rohling, and Thomas F. Stocker

The last glacial cycle provides the opportunity to investigate large changes in the Atlantic Meridional Overturning Circulation (AMOC) beyond the small fluctuations evidenced from direct measurements. Paleotemperature records from Greenland and the North Atlantic show an abrupt variability, called Dansgaard–Oeschger (DO) events, which is associated with abrupt changes of the AMOC. These DO events also have Southern Hemisphere counterparts via the thermal bipolar seesaw, a concept describing the meridional heat transport leading to asynchronous temperature changes between both hemispheres. However, temperature records from the North Atlantic show more pronounced DO cooling events during massive releases of icebergs known as Heinrich (H) events, contrary to ice-core–based temperature records from Greenland. Here, we present high-resolution temperature records from the Iberian Margin and a Bipolar Seesaw Index to discriminate DO cooling events with and without H events. We show that the thermal bipolar seesaw model generates synthetic Southern Hemisphere temperature records that best resemble Antarctic temperature records when using temperature records from the Iberian Margin as inputs. Our data-model comparison emphasizes the role of the thermal bipolar seesaw in the abrupt temperature variability of both hemispheres with a clear enhancement during DO cooling events with H events, implying a relationship that is more complex than a simple flip-flop between two climate states linked to a tipping point threshold.

bipolar seesaw | abrupt climate changes | paleotemperature | paleoceanography

Significance

The evolution of the Atlantic Meridional Overturning Circulation remains difficult to constrain from direct measurements. During the last glacial cycle, the strength of this circulation covaried with temperature in the North Atlantic, itself connected to Southern Hemisphere temperature. However, this interhemispheric connection was mostly studied using Greenland and Antarctic ice cores, resulting in an incomplete picture of the thermal bipolar seesaw. Using new temperature records from the Iberian Margin, a new Bipolar Seesaw Index, and Southern Hemisphere temperature simulations, we discriminate Northern Hemisphere cold events with and without massive iceberg discharges into the North Atlantic. Our data-model comparison implies a relationship that is more complex than a simple flip-flop between two climate states linked to a tipping point threshold.

Evidence has been growing for systematic changes of the Atlantic Meridional Overturning Circulation (AMOC) over the past decades (1, 2). An AMOC decreasing shift may contribute to the "warming hole" observed in the surface temperature of the North Atlantic, a feature in data and model simulations that has been interpreted as a complex oceanic response to rising CO_2 in the atmosphere (2, 3). Projections based on numerical models show that AMOC weakening will continue to accompany global warming due to the forthcoming emissions of anthropogenic CO_2 (4). Nevertheless, the existence and amplitude of the long-term trend in recent observations remain a subject of debate due to large high-frequency AMOC variability (1, 5). In addition, the future evolution of the AMOC and its dependence on the overall amplitude and rapidity of future scenarios of anthropogenic forcing are still very uncertain (4, 6).

Geochemical studies of deep-sea cores have shown that the AMOC was particularly variable during the last glacial cycle, in apparent synchrony with the temperature record in the same North Atlantic sediments (7–12) and in Greenland ice cores (13, 14). Several cold events of the abrupt Dansgaard–Oeschger (DO) variations, named DO stadials (15–17), also correspond to massive releases of icebergs into the North Atlantic—Heinrich (H) events—as testified by layers of ice-rafted debris (IRD) found in deep-sea cores (14, 18). Indeed, the H and DO events provide the best record for studying large changes of the AMOC on time scales from decades to millennia.

Decades of work have strengthened the knowledge of H and DO variations in the North Atlantic and surrounding continents, including Greenland with its highly detailed paleotemperature records based on the water and gas isotopes measured in ice cores (Figs. 1 *A* and *B* and 2*A*; see *SI Appendix*, Text S1 for details). Nevertheless, there is an important contrast between the shapes of North Atlantic sea surface temperature (SST) and Greenland temperature records during some abrupt climate changes, namely the difference in relative amplitude of coolings during DO stadials with and without H events (19).

A clear illustration of the amplitude difference between Greenland and Atlantic records is provided by the youngest and best-known Heinrich event 1 (H1). Indeed, during H1 the oxygen isotope composition of ice—$\delta^{18}O_{ice}$, an index positively correlated with atmospheric temperature—is even higher than during other DO stadials and the last glacial cold spell called the Younger Dryas event, both in the GRIP and GISP2 Greenland Summit cores and in earlier cores from other sites such as Dye 3 and Camp Century (34, 35).

Author contributions: E.B. designed research; N.D. and E.B. performed research; N.D. analyzed data; and N.D. and E.B. wrote the paper.

Reviewers: J.F.M., Columbia University; E.J.R., Australian National University; and T.F.S., Universitat Bern.

The authors declare no competing interest.

[1]Present address: Institut de Ciència i Tecnologia Ambientals, Universitat Autònoma de Barcelona, Cerdanyola del Vallès, Barcelona 08193, Spain.

[2]To whom correspondence may be addressed. Email: Nina.Davtian@uab.cat or bard@cerege.fr.

This article contains supporting information online at https://www.pnas.org/lookup/suppl/doi:10.1073/pnas.2209558120/-/DCSupplemental.

Published March 13, 2023.

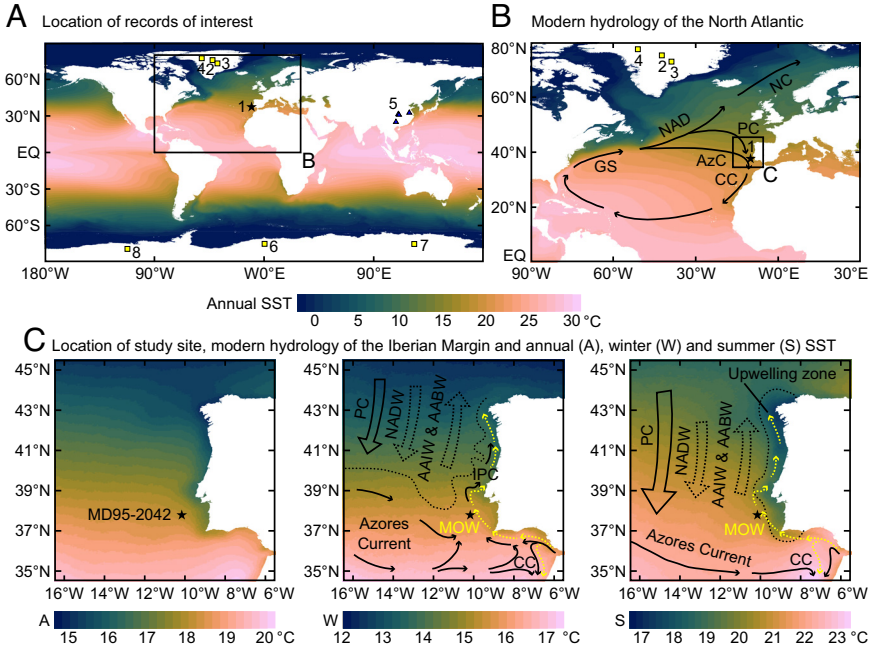

Fig. 1. Location and modern hydrology of the core MD95-2042 site in the Iberian Margin. (*A*) Location of records mentioned in the text. (1) Core MD95-2042, (2) NGRIP, (3) GISP2, (4) NEEM, (5) Chinese speleothems, (6) EDML, (7) EDC, and (8) WD. The Chinese speleothem records indicated are those compiled by ref. 20. (*B*) North Atlantic. (*C*) Iberian Margin and core MD95-2042. Solid arrows represent surface currents, whereas dotted arrows represent deep currents. GS, Gulf Stream; NAD, North Atlantic Drift; NC, Norwegian Current; PC, Portugal Current; AzC, Azores Current; CC, Canary Current; IPC, Iberian Poleward Current; MOW, Mediterranean Outflow Waters; NADW, North Atlantic Deep Waters; AAIW, Antarctic Intermediate Waters; and AABW, Antarctic Deep Waters. The colored SST gradients represent Pathfinder SST V5 climatology at 4-km resolution (21, 22). Modified from ref. 23.

Moreover, quantitative paleotemperature reconstructions based on $\delta^{15}N$ in Greenland ice confirm this lack of enhanced cooling during DO stadials with H events—named H stadials hereafter—when compared to other DO stadials (25) (Fig. 2*A*).

Previous modeling work indicates that Greenland may have been insulated from further cooling during H stadials due to a southward shift of North Atlantic Deep Water formation zones (36) and to the presence of sea ice surrounding Greenland (37–39). More recent modeling studies suggest that the lack of response in Greenland may be due to seasonal effects on the $\delta^{18}O_{ice}$ proxy (40). None of these effects are mutually exclusive and any of them could have acted in concert to bias the Greenland record but not the Iberian Margin record which has probably captured the true regional signal of the North Atlantic.

Numerical models perturbed by freshwater input into the North Atlantic have been used to mimic the massive iceberg release during H events (19, 36, 41–44). This usually leads to a strong AMOC decrease or even a collapse, with global impacts on surface temperatures, notably an intense cooling in the North Atlantic and surrounding continents and a moderate warming in the Southern Hemisphere. The robust behavior of these numerical models of varying complexity (19, 36, 41–44) has led to the notion of the thermal bipolar seesaw, which has been simplified as a thermal system that couples a southern heat reservoir with the Atlantic Ocean and which links both hemispheres (45).

The thermal bipolar seesaw model was used to study amplitude differences between paleotemperature records reconstructed from Greenland and Antarctic ice cores (46). This comparison led to the discovery of a one-to-one coupling between Antarctic warm events, named Antarctic Isotope Maximum (AIM) events, and Greenland cold events (30, 31, 47–51), with a strong correlation between the amplitude of Antarctic warmings (ΔT_s) and the duration of Greenland coolings (Δt_n) (30).

Nevertheless, the comparison between Greenland and Antarctic temperature records, by means of the ΔT_s versus Δt_n diagram and the thermal bipolar seesaw model, is not fully satisfactory because the northern component of the thermal seesaw should be represented with North Atlantic temperatures, rather than with those over Greenland, whose record is truncated during H stadials (Fig. 2*A*). Indeed, the sole use of the DO stadial duration (Δt_n) in the correlation diagram implicitly assumes that amplitude changes of northern DO stadials (ΔT_n) are negligible or irrelevant, which is not true for North Atlantic SST records (19). A possible impact of the enhanced cooling during H stadials on the thermal bipolar seesaw has been tested in several studies, but inconclusive and conflicting results were obtained (52–54).

In order to revisit this question, we reconstruct a North Atlantic SST record over the entire last glacial cycle by reanalyzing at high resolution the well-known core MD95-2042 from the Iberian Margin (see location in Fig. 1 and *Materials and Methods*) with the Ring Index of hydroxylated tetraethers with OH-GDGT-0 (RI-OH′) paleothermometric proxy (Fig. 2*B*), in comparison with the unsaturation index of alkenones (U^{K}_{37}) record (Fig. 2*C*) measured in the very same samples (*Materials and Methods*) and the ice-volume–corrected planktic foraminiferal $\delta^{18}O$ record (*SI Appendix*, Fig. S1*B*)—see *SI Appendix*, Text S1 and Figs. S1 and S2 for details and motivations concerning our selection of Iberian Margin SST records. We also update the chronology of core MD95-2042 by considering the most recent geochronological improvements over the last glacial cycle—e.g., the IntCal20 calibration over the ^{14}C range (55) (*SI Appendix*, Table S1 and *Materials and Methods*).

Our study follows two complementary approaches. First, our SST records from the Iberian Margin have a temporal resolution suitable for the detection of H and DO stadials and for use as input curves for the thermal bipolar seesaw model, in complement to Greenland ice-core records. We thus revisit the classical ΔT_s versus Δt_n diagram and the thermal bipolar seesaw model using better-dated and better-resolved SST records from the

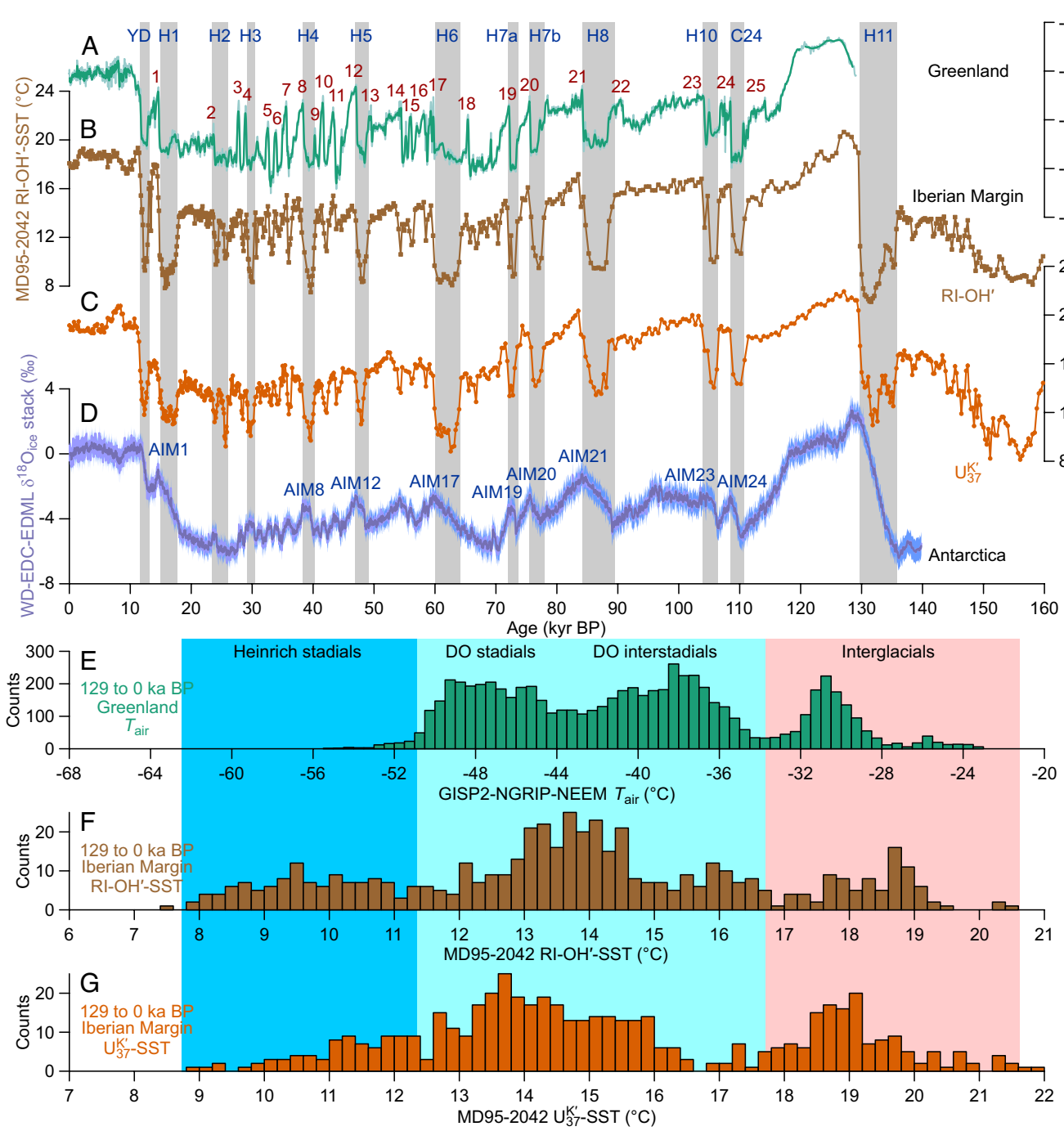

Fig. 2. The separation between Heinrich stadials and other Dansgaard–Oeschger stadials during the last climatic cycle. (*A*) Greenland T_{air} records from the GISP2 (24), NGRIP (25), and NEEM (26) ice cores. NEEM T_{air} values were obtained by adding –31 °C to published anomalies. (*B*) RI-OH′-SST record from core MD95-2042 (*Materials and Methods*; partly published in ref. 23). (*C*) $U^{K'}_{37}$-SST record from core MD95-2042 (23, 27). See also *Materials and Methods*. (*D*) Antarctic stack of the $\delta^{18}O_{ice}$ records from EDC (28, 29), EDML (28, 30), and WD (31–33) over the 140 to 0 ka BP period with its 2σ confidence interval (CI) (*Materials and Methods*). See Fig. 1 for record locations and *Materials and Methods* for chronologies. (*E*–*G*) Histograms of Greenland T_{air} and core MD95-2042 RI-OH′-SST and $U^{K'}_{37}$-SST values, respectively, over the 129 to 0 ka BP period. For the GISP2 portion of the Greenland T_{air} record, subsampled 10-point averages were used instead of published values to limit overrepresentation of the Holocene. Gray bars with labels in *A*–*D* indicate the Younger Dryas and Heinrich and Heinrich-like stadials. Numbers in *A* indicate Dansgaard–Oeschger events. Labels in *D* indicate Antarctic Isotope Maximum events occurring during Heinrich and Heinrich-like stadials.

Iberian Margin and paleothermometric records from ice cores in Greenland and Antarctica. Second, we revisit relationships between DO stadials and AIM events by considering two Southern versus Northern Hemisphere diagrams extended from the classical ΔT_s versus Δt_n diagram. This extension allows us to introduce a climatic index useful to differentiate and highlight the thermal bipolar seesaw impact for different types of DO stadials.

Results and Discussion

Iberian Margin RI-OH′ SST Record from Core MD95-2042. Core MD95-2042 (37°45′N, 10°10′W, 3,146 m water depth; Fig. 1) was retrieved from the distal part of the Iberian Margin continental slope during the IMAGES I (1995) cruise of R/V Marion Dufresne using a Calypso corer. The coring site was chosen to replicate and extend the shorter piston core SU8118 (37°46′N, 10°11′W, 3,135 m water

depth) used in previous studies (56, 57). The core MD95-2042 site is located at the edge of the upwelling area, roughly 150 km from the modern coastline—see *SI Appendix*, Text S1 for details on the environmental context. The sediment core is 3,140 cm long, covers the last 160 ky, and mainly consists of calcareous silty clay. Here, we extend the core MD95-2042 tetraether-based records acquired by ref. 23, including the RI-OH′ record on which we focus so that they cover the last 160 ky (*Materials and Methods*).

Our Iberian Margin RI-OH′ SST record faithfully shows DO events with contrasting cooling amplitudes between H stadials and other DO stadials (Fig. 2*B*), independently from established SST proxies such as $U^{K'}_{37}$—see *SI Appendix*, Text S2 and Figs. S3–S5 for a discussion on the independence of RI-OH′ as an SST proxy. Contrary to the Greenland atmospheric temperature (T_{air}) record (Fig. 2 *A* and *E*), the Iberian Margin RI-OH′ record gives cooler SSTs during H stadials than during other DO stadials (Fig. 2 *B* and *F*), as is the case for the Iberian Margin $U^{K'}_{37}$ record from the same core (Fig. 2 *C* and *G*). These patterns further strengthen a previous validation of RI-OH′ as an SST proxy in the Iberian Margin (23). The increased temporal resolution of the biomarker-based Iberian Margin SST records and their faithful capture of enhanced cooling during H stadials thus support further analysis of the thermal bipolar seesaw using these Iberian Margin SST records, including the RI-OH′ SST record.

General Approach. We group DO stadials into three categories for all studied Southern versus Northern hemisphere diagrams: 1) H stadials with an IRD layer in core MD95-2042 and other North Atlantic sediments, 2) H stadials without an IRD layer in core MD95-2042 sediments, named H-like events by ref. 58 and H-like stadials hereafter, and 3) other DO stadials. We provide further details on the nomenclature in *Materials and Methods*.

We essentially compare SST records from the Iberian Margin with ice-core paleothermometric records from Antarctica to revisit the thermal bipolar seesaw—we also consider and discuss SST records from the Southern Ocean in *SI Appendix*, Text S3 and Fig. S6. In parallel, we compare ice-core records from Greenland and Antarctica (*Materials and Methods*). We mainly use normalized temperature records expressed in unit standard deviation (SD) over the 129 to 0 thousand years before present (ka BP, where 0 ka BP is 1950 CE) period (*Materials and Methods*)—see *SI Appendix*, Text S5 and Fig. S10 for a test using nonnormalized temperature records and other motivations of our temperature record normalizations. We thus focus on the shapes of temperature records, i.e., relative changes rather than actual temperature values, which depend on uncertain calibrations for the various proxies (23, 25, 59, 60). Our analysis thus relies on the assumption of monotonous proxy-temperature relationships.

For all studied Southern versus Northern hemisphere diagrams, we calculate Pearson's *r* coefficients for comparison with previous thermal bipolar seesaw studies (30, 47, 48, 54) and Kendall's τ rank coefficients for robust correlation tests, notably for nonnormally distributed input values. We use the 95% level—$P < 0.05$—as the significance criterion for interhemispheric relationships. We follow a Monte Carlo method modified from ref. 54 to assess the influence of nonsystematic temperature uncertainties on our results (*Materials and Methods*)—we do not include chronological uncertainties, given their multiple and archive-dependent sources, as discussed in detail in *SI Appendix*, Text S6. We also follow a bootstrapping method to compare absolute correlation coefficient values between Greenland and Iberian Margin temperature records as Northern Hemisphere components (*Materials and Methods*).

For all applications of the thermal bipolar seesaw model (*Materials and Methods*, ref. 46), we use three goodness-of-fit metrics for model versus data comparisons: Pearson's *r* coefficient for comparison with previous thermal bipolar seesaw studies (46, 52), Kendall's τ rank coefficient for robust correlation tests, notably for input values with nonnormal distributions, and mean squared error (MSE) to take advantage of residuals with normal distributions. We express the records in unit SD over the 115 to 12 ka BP period to concentrate on the shape of changes, as for Southern versus Northern Hemisphere diagrams. Similarly, we assess the influence of nonsystematic temperature uncertainties on model versus data comparisons using a Monte Carlo method modified from ref. 54 without chronological uncertainties for simplicity (*Materials and Methods* and *SI Appendix*, Text S6). We outline all statistical and uncertainty results from this study in *SI Appendix*, Table S2.

Classical Southern versus Northern Hemisphere Diagram. We reevaluate the classical ΔT_s versus Δt_n relationship between DO stadials and AIM events using our Iberian Margin RI-OH′ SST record as the Northern Hemisphere component and a $\delta^{18}O_{ice}$ stack from Antarctic ice cores as the Southern Hemisphere component (*Materials and Methods*)—see *SI Appendix*, Table S3 for results from other Southern and Northern Hemisphere paleothermometric records. Our Antarctic $\delta^{18}O_{ice}$ stack and Iberian Margin RI-OH′ SST record give a strong ΔT_s versus Δt_n relationship when all Dansgaard–Oeschger stadial-Antarctic Isotope Maximum (DO-AIM) pairs are considered—$r = 0.73$ and $\tau = 0.51$, $P < 0.001$ for both correlation tests (Fig. 3*A*; see also *SI Appendix*, Text S7 and Tables S4, S5, and S15 for comparisons of classical ΔT_s versus Δt_n relationships). Most DO-AIM pairs follow a linear ΔT_s versus Δt_n relationship close to a regression line through the origin which considers errors in both coordinates (Fig. 3*A*)—the thermal bipolar seesaw model (46) motivates regression lines with intercepts forced to 0 for all Southern versus Northern Hemisphere diagrams.

We assess how well DO-AIM pairs follow our linear ΔT_s versus Δt_n relationship. The DO-AIM pairs 2b and 18 deviate from our linear ΔT_s versus Δt_n relationship (Fig. 3*A*), similarly to the DO-AIM pairs 2 and 18 in ref. 48 which deviate from the original ΔT_s versus Δt_n relationship by ref. 30—ref. 48 did not include the DO-AIM pairs 14 and 17 which deviate from our linear ΔT_s versus Δt_n relationship (Fig. 3*A*). Conversely, the DO-AIM pair 21 follows our linear ΔT_s versus Δt_n relationship (Fig. 3*A*), contrary to the same DO-AIM pair in refs. 47 and 48 which deviates from the original ΔT_s versus Δt_n relationship by ref. 30. Yet, the DO-AIM pair 21 deviates from most other DO-AIM pairs when considering the Greenland record rather than our Iberian Margin record (*SI Appendix*, Fig. S11). Similarly, our regression line misfits with most DO-AIM pairs when considering the Greenland record rather than our Iberian Margin record, although the DO-AIM pair 21 deviates little from our regression line in both cases (*SI Appendix*, Fig. S11). While the linear regression in ref. 30—established using the ordinary least squares method—captures most DO-AIM pairs in refs. 47 and 48, our regression method better supports the linear ΔT_s versus Δt_n relationship when considering our Iberian Margin record than when considering the Greenland record (Fig. 3*A* and *SI Appendix*, Fig. S11). Therefore, our Iberian Margin SST record provides a stronger confirmation of the thermal bipolar seesaw than does the Greenland T_{air} record.

Thermal Bipolar Seesaw Model Simulations. We use both biomarker-based Iberian Margin SST records (RI-OH′ and $U^{K'}_{37}$) and the Greenland T_{air} (25) and $\delta^{18}O_{ice}$ (13) records as inputs for the thermal bipolar seesaw model (*Materials and Methods*, ref.

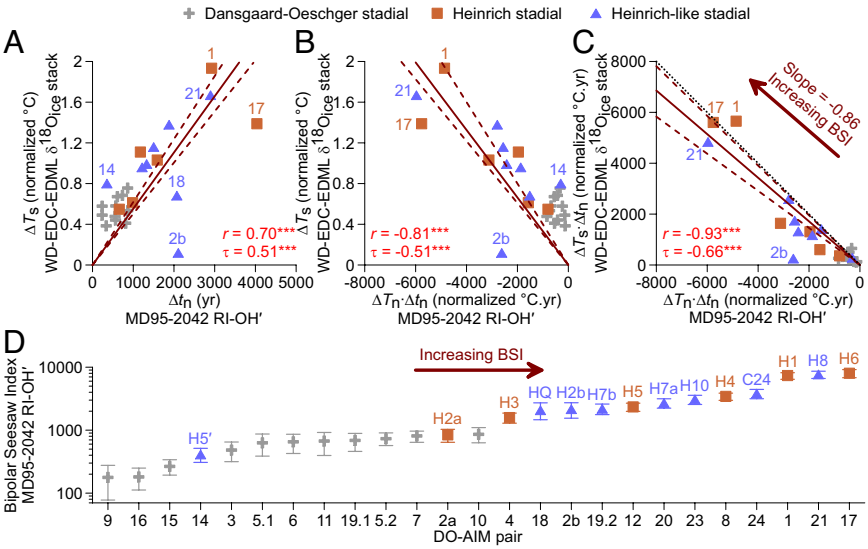

Fig. 3. The relationship between Southern and Northern Hemisphere climate events from the perspective of the Iberian Margin RI-OH′ SST record. (*A*) Classical ΔT_s versus Δt_n diagram. (*B*) Extended ΔT_s versus $\Delta T_n \bullet \Delta t_n$ diagram. (*C*) Extended $\Delta T_s \bullet \Delta t_n$ versus $\Delta T_n \bullet \Delta t_n$ diagram (*Materials and Methods*). Only the end-member scenario that best depicts the thermal bipolar seesaw (Scenario 1; see *SI Appendix*, Text S8) is shown here. The Southern Hemisphere record used in all cases is an Antarctic stack of the $\delta^{18}O_{ice}$ records from EDC (28, 29), EDML (28, 30), and WD (31–33) over the 140 to 0 ka BP period (*Materials and Methods*). Both Southern and Northern Hemisphere have been centered to zero means and normalized to unit SDs over the 129 to 0 ka BP period. Labels indicate a few Dansgaard–Oeschger stadial-Antarctic Isotope Maximum (DO-AIM) pairs, as per refs. 30, 47, and 48—see *SI Appendix*, Fig. S11 for the identification of all DO-AIM pairs. Antarctic Isotope Maximum events with Heinrich and Heinrich-like stadials are distinguished from Antarctic Isotope Maximum events with other Dansgaard–Oeschger stadials. Solid lines represent regression lines with intercepts forced to 0 and which considers errors in both coordinates (*Materials and Methods*). Dashed lines represent 95% CIs of regression slopes from 1,000 Monte Carlo iterations (*Materials and Methods*). The dotted line in *C* represents the –1:1 line. For the sake of readability, error bars for individual data points in *A*–*C* are omitted here and shown in *SI Appendix*, Fig. S12. Pearson's *r* coefficients and Kendall's τ rank coefficients are also shown in *A*–*C*, with their 99.9% significance levels coded as ***. (*D*) Bipolar Seesaw Index (BSI) values (*Materials and Methods*). Given the wide amplitude between the highest and lowest BSI values, the *y* axis has a logarithmic scale. Each DO-AIM pair has the same symbol as in *A*–*C*. Colored labels indicate Heinrich and Heinrich-like stadials.

46). We then compare each bipolar seesaw output (BSO) using our Antarctic $\delta^{18}O_{ice}$ stack as the Southern Hemisphere reference record (*SI Appendix*, Texts S10–S13). To circumvent uncertainties due to partially independent ice-core and core MD95-2042 chronologies—see *SI Appendix*, Text S6 for details—we also compare the BSOs from the three Iberian Margin SST records (RI-OH′, $U^{K'}_{37}$, and ice-volume–corrected planktic foraminiferal $\delta^{18}O$) with the ice-volume–corrected benthic foraminiferal $\delta^{18}O$ record from the same Iberian Margin sediment core—see *SI Appendix*, Text S14 for details.

All BSO records for the 115 to 12 ka BP period are visually and statistically in good agreement with the Southern Hemisphere reference record (Fig. 4*A* and *SI Appendix*, Table S16)—e.g., *r* values between 0.52 and 0.63 and τ values between 0.33 and 0.44 over the 115 to 12 ka BP period (*SI Appendix*, Table S16). Visually, the BSOs from Iberian Margin SST records also better

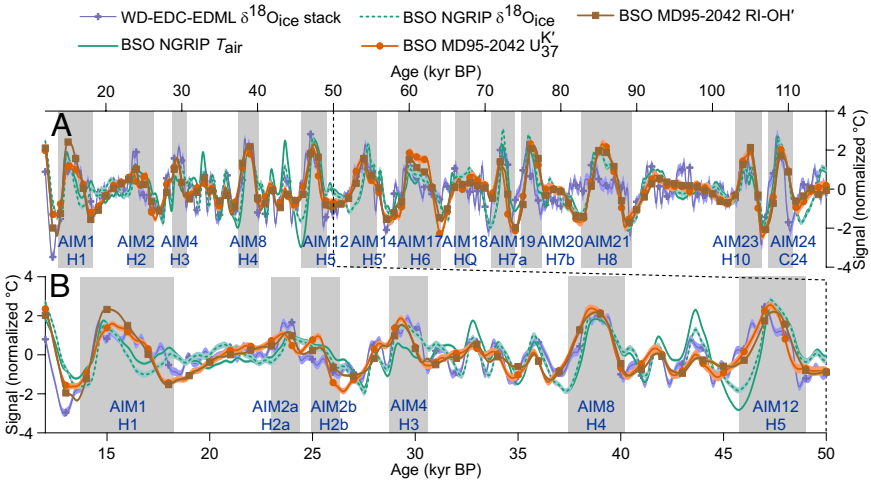

Fig. 4. Comparison between bipolar seesaw model outputs from several Northern Hemisphere temperature records and a Southern Hemisphere reference record. (*A*) 115- to 12-ka BP period using a band-pass filter with a 500- to 10,000-y window. (*B*) Close up of the 50- to 12-ka BP period. Each bipolar seesaw output (BSO) and reference record has been centered to zero means and normalized to unit SDs over the 115 to 12 ka BP period in *A* and over the 50 to 12 ka BP period in *B* to facilitate the comparison (*Materials and Methods*). Shading around BSO and reference records in both *A* and *B* represents their 95% CIs from 1,000 Monte Carlo iterations (*Materials and Methods*). The Southern Hemisphere reference record is an Antarctic stack of the $\delta^{18}O_{ice}$ records from EDC (28, 29), EDML (28, 30), and WD (31–33) over the 140 to 0 ka BP period (*Materials and Methods*). Gray bars with labels indicate Antarctic Isotope Maximum events with Heinrich and Heinrich-like stadials.

agree with the Southern Hemisphere reference record than do the BSOs from Greenland paleothermometric records, especially for the second half of the last glacial cycle (Fig. 4*B*). Indeed, Iberian Margin BSOs mostly show significantly better fits (Pearson's r, Kendall's τ, and MSE) than Greenland BSOs do at the 95% level (*SI Appendix*, Fig. S13, Table S17, and Text S11).

Reference SST records for the North Atlantic are based on $U^{K'}_{37}$, the most established organic paleothermometer off the southern Iberian Margin (23, 27, 57, 61, 62) (Fig. 2*C*). The recent RI-OH′ organic paleothermometer further confirms that the southern Iberian Margin is an ideal place to investigate North Atlantic SSTs (23) (Fig. 2*B*). The BSO from the RI-OH′ record even has some significantly better agreements with the Southern Hemisphere reference record than does the BSO from the $U^{K'}_{37}$ record at the 95% level (*SI Appendix*, Table S17).

The Iberian Margin SST records generate Southern Hemisphere temperature simulations that are in good agreement with the Antarctic record—e.g., r values of 0.59 and 0.63 and τ values of 0.42 and 0.44 over the 115 to 12 ka BP period (*SI Appendix*, Table S16). Indeed, the BSOs from both biomarker-based Iberian Margin SST records show particularly strong AIM amplitudes during H6 to H3 and H1 as well as during H-like stadials such as C24, H10, and H8 (58), which is not the case for the BSOs from both Greenland paleothermometric records (Fig. 4). Despite their better resolutions compared with the Iberian Margin SST records (Fig. 2 *A*–*C*), the Greenland T_{air} and $\delta^{18}O_{ice}$ records do not generate better Southern Hemisphere temperature simulations (Fig. 4 and *SI Appendix*, Fig. S13 and Table S17). Discrepancies between the Southern Hemisphere reference record and BSOs from Greenland records occur, for instance, at ca. 112, 94, and 57 ka BP and during H5 to H3 and H1 (Fig. 4).

We then jointly use the classical ΔT_s versus Δt_n diagram and synthetic Southern Hemisphere records generated by forcing the thermal bipolar seesaw model with biomarker-based Iberian Margin SST records and Greenland T_{air} and $\delta^{18}O_{ice}$ records (*SI Appendix*, Tables S7–S14). Contrary to observed temperature records, filtered and simulated temperature records give typically weak to nonsignificant ΔT_s versus Δt_n relationships, except when using Southern Hemisphere temperature records simulated from the Iberian Margin SST records (*SI Appendix*, Tables S7 and S11). Furthermore, Southern Hemisphere temperature records simulated from the Greenland paleothermometric records systematically give weak and nonsignificant ΔT_s versus Δt_n relationships—r values between 0.10 and 0.30 and τ values between 0.16 and 0.27—whereas Southern Hemisphere temperature records simulated from the Iberian Margin SST records systematically give moderate-to-strong and significant ΔT_s versus Δt_n relationships—r values between 0.48 and 0.74 and τ values between 0.38 and 0.55 ($P < 0.02$ for all correlation tests; *SI Appendix*, Tables S7 and S11). Overall, our combined use of classical ΔT_s versus Δt_n diagrams with the thermal bipolar seesaw model further supports the relevance of North Atlantic SST records such as those from the Iberian Margin to study the thermal bipolar seesaw, in conjunction with Greenland and Antarctic ice-core paleothermometric records.

Extended Southern versus Northern Hemisphere Diagrams. We propose two extensions of the classical ΔT_s versus Δt_n diagram to consider the contrasting cooling amplitudes (ΔT_n) between H stadials and other DO stadials for Iberian Margin SST records, namely the ΔT_s versus $\Delta T_n{\cdot}\Delta t_n$ and $\Delta T_s{\cdot}\Delta t_n$ versus $\Delta T_n{\cdot}\Delta t_n$ diagrams. Like the classical ΔT_s versus Δt_n diagram, our extended ΔT_s versus $\Delta T_n{\cdot}\Delta t_n$ diagram relies on the physical basis of the thermal bipolar seesaw for which an approximation links ΔT_s, ΔT_n, and Δt_n:

$$\Delta T_s \approx \left(\frac{\Delta T_n}{2T}\right)\cdot \Delta t_n, \qquad [1]$$

with T the time characteristic of the heat reservoir involved in the thermal bipolar seesaw model (46)—Equation 1 is Equation 9.5 on page 162 in ref. 63. This approximation implies that a linear correlation is expected in the ΔT_s versus Δt_n space, only if the term in parenthesis ($\Delta T_n/2T$) is broadly constant. This is justified for Greenland and is the reason for the strong linear dependence described in ref. 30. However, Eq. **1** clearly illustrates that the Southern Hemisphere warming also depends on the overall cooling ΔT_n in the Northern Hemisphere, which is variable in North Atlantic SST records (19) by contrast to Greenland temperature records. The elegance of the extended ΔT_s versus $\Delta T_n{\cdot}\Delta t_n$ diagram is that the relationship linking ΔT_s, and $\Delta T_n{\cdot}\Delta t_n$ depends solely on 1/2T rather than on $\Delta T_n/2T$ for the classical ΔT_s versus Δt_n diagram.

In addition, we calculate the $\Delta T_n{\cdot}\Delta t_n$ product that would be proportional to the accumulated heat loss within the Northern Hemisphere during the time Δt_n when the AMOC is weaker. Similarly, the $\Delta T_s{\cdot}\Delta t_n$ product would be proportional to the accumulated heat gain within the Southern Hemisphere during the time Δt_n when the AMOC is weaker. This justifies the use of our second extended diagram, $\Delta T_s{\cdot}\Delta t_n$ versus $\Delta T_n{\cdot}\Delta t_n$ representative of the heat exchange between both hemispheres. We provide a more detailed physical basis and motivation of our extended ΔT_s versus $\Delta T_n{\cdot}\Delta t_n$ and $\Delta T_s{\cdot}\Delta t_n$ versus $\Delta T_n{\cdot}\Delta t_n$ diagrams in *SI Appendix*, Text S4 and Figs. S7–S10.

We use our Iberian Margin RI-OH′ SST record as the Northern Hemisphere component and our Antarctic $\delta^{18}O_{ice}$ stack as the Southern Hemisphere component (*Materials and Methods*) to evaluate ΔT_s versus $\Delta T_n{\cdot}\Delta t_n$ and $\Delta T_s{\cdot}\Delta t_n$ versus $\Delta T_n{\cdot}\Delta t_n$ relationships between DO stadials and AIM events—see *SI Appendix*, Table S3 for results from other Southern and Northern Hemisphere paleothermometric records. Our Antarctic $\delta^{18}O_{ice}$ stack and our Iberian Margin RI-OH′ SST record give strong ΔT_s versus $\Delta T_n{\cdot}\Delta t_n$ and $\Delta T_s{\cdot}\Delta t_n$ versus $\Delta T_n{\cdot}\Delta t_n$ relationships when all DO-AIM pairs are considered—$r = -0.81$ and $\tau = -0.51$ for ΔT_s versus $\Delta T_n{\cdot}\Delta t_n$ diagrams (Fig. 3*B*), and $r = -0.93$ and $\tau = -0.66$ for $\Delta T_s{\cdot}\Delta t_n$ versus $\Delta T_n{\cdot}\Delta t_n$ diagrams (Fig. 3*C*), $P < 0.001$ for all correlation tests.

Our extended $\Delta T_s{\cdot}\Delta t_n$ versus $\Delta T_n{\cdot}\Delta t_n$ diagram shows the strongest relationship, not only for our Antarctic $\delta^{18}O_{ice}$ stack paired with our Iberian Margin RI-OH′ SST record (Fig. 3) but also for all other pairs of Southern and Northern Hemisphere paleothermometric records (*SI Appendix*, Fig. S11 and Table S3). These correlation results are coherent with those obtained from idealized Antarctic and Iberian Margin temperature records—see *SI Appendix*, Text S4 for details. Most DO-AIM pairs follow linear relationships close to regression lines through the origin which consider error in both coordinates for our extended ΔT_s versus $\Delta T_n{\cdot}\Delta t_n$ and $\Delta T_s{\cdot}\Delta t_n$ versus $\Delta T_n{\cdot}\Delta t_n$ diagrams (Fig. 3 *B* and *C*). While the classical ΔT_s versus Δt_n diagram and our extended ΔT_s versus $\Delta T_n{\cdot}\Delta t_n$ diagram show linear relationships that involve the time characteristic of the heat reservoir, our extended $\Delta T_s{\cdot}\Delta t_n$ versus $\Delta T_n{\cdot}\Delta t_n$ diagram gives regression slopes that would reflect the heat distribution between both hemispheres—see *SI Appendix*, Text S9 for interpretations of the $\Delta T_s{\cdot}\Delta t_n$ versus $\Delta T_n{\cdot}\Delta t_n$ slopes and a test with AIM warming areas integrated from cyclic and idealized Southern Hemisphere temperature records.

Our extended ΔT_s versus $\Delta T_n \cdot \Delta t_n$ and $\Delta T_s \cdot \Delta t_n$ versus $\Delta T_n \cdot \Delta t_n$ diagrams only have a few DO-AIM pairs that prominently deviate from the linear relationships, notably the DO-AIM pair 2b (Fig. 3 *B* and *C* and *SI Appendix*, Fig. S11). This systematic deviation is due to our use of similar DO stadial 2b delimitations for all Northern Hemisphere paleothermometric records, as H2b has a much shorter duration in the Iberian Margin than DO stadial 2b in Greenland (*SI Appendix*, Fig. S14). Accordingly, the DO-AIM pair 2b would be closer to the DO-AIM pair 2a for the Iberian Margin, notably our RI-OH′ SST record which has similar DO coolings for both H2 subevents. The DO-AIM pair 18 still deviates from linear ΔT_s versus $\Delta T_n \cdot \Delta t_n$ and $\Delta T_s \cdot \Delta t_n$ versus $\Delta T_n \cdot \Delta t_n$ relationships when considering Greenland rather than the Iberian Margin (*SI Appendix*, Fig. S11). Despite these few deviations, our extended ΔT_s versus $\Delta T_n \cdot \Delta t_n$ and $\Delta T_s \cdot \Delta t_n$ versus $\Delta T_n \cdot \Delta t_n$ diagrams are relevant for studying the thermal bipolar seesaw, notably using paleothermometric records with contrasting cooling amplitudes between H stadials and other DO stadials such as Iberian Margin SST records.

Our joint use of extended Southern versus Northern Hemisphere diagrams and synthetic Southern Hemisphere records generated by forcing the thermal bipolar seesaw model with biomarker-based Iberian Margin SST records and Greenland T_{air} and $\delta^{18}O_{ice}$ records (*SI Appendix*, Tables S7–S14) reveals typically weak to nonsignificant ΔT_s versus $\Delta T_s \cdot \Delta t_n$ relationships, except when using Southern Hemisphere temperature records simulated from the Iberian Margin SST records (*SI Appendix*, Tables S7 and S11). Our extended ΔT_s versus $\Delta T_s \cdot \Delta t_n$ diagram also shows stronger relationships when using Southern Hemisphere temperature records simulated from the Iberian Margin SST records than when using those simulated from the Greenland paleothermometric records (*SI Appendix*, Tables S7 and S11). Conversely, our extended $\Delta T_s \cdot \Delta t_n$ versus $\Delta T_n \cdot \Delta t_n$ diagram systematically shows strong and significant relationships when using filtered and simulated temperature records—*r* values between –0.69 and –0.97 and τ values between –0.46 and –0.88 ($P < 0.001$ for almost all correlation tests under both end-member scenarios; *SI Appendix*, Text S8 and Tables S7 and S11). Overall, our combined use of Southern versus Northern Hemisphere diagrams with the thermal bipolar seesaw model further supports the relevance of our extended ΔT_s versus $\Delta T_n \cdot \Delta t_n$ and $\Delta T_s \cdot \Delta t_n$ versus $\Delta T_n \cdot \Delta t_n$ diagrams to study the thermal bipolar seesaw using North Atlantic SST records and Greenland and Antarctic ice-core paleothermometric records, in conjunction with the classical ΔT_s versus Δt_n diagram.

Interhemispheric Relationships for Restricted Populations of DO-AIM Pairs. We only use our extended $\Delta T_s \cdot \Delta t_n$ versus $\Delta T_n \cdot \Delta t_n$ diagram for statistical analyses restricted to populations of DO-AIM pairs, given the typical losses of significance at the 95% level for the other Southern versus Northern Hemisphere diagrams due to reduced numbers of events (*SI Appendix*, Tables S6, S10, and S14). When considering the population of H and H-like stadials, most $\Delta T_s \cdot \Delta t_n$ versus $\Delta T_n \cdot \Delta t_n$ relationships remain strong and significant at the 95% level, despite the reduced dynamic range in the restricted population. However, $\Delta T_s \cdot \Delta t_n$ versus $\Delta T_n \cdot \Delta t_n$ relationships are less robust to restrictions to the population of other DO stadials, given the more frequent losses of significance at the 95% level (*SI Appendix*, Tables S6, S10, and S14). This contrast in losses of significance is likely due to the contrasting thermal bipolar seesaw responses between H and H-like stadials and other DO stadials. Overall, our statistical analysis for restricted populations of DO-AIM pairs may support the existence of at least three glacial modes (64) or even continuous thermal bipolar seesaw responses scaled to the forcing during H stadials.

Bipolar Seesaw Index (BSI). Our Iberian Margin RI-OH′ SST record provides a clear illustration of the relevance of our extended $\Delta T_s \cdot \Delta t_n$ versus $\Delta T_n \cdot \Delta t_n$ diagram—*r* value of –0.93 and τ value of –0.66—in parallel with the strong relationships in ΔT_s versus Δt_n and ΔT_s versus $\Delta T_n \cdot \Delta t_n$ diagrams—*r* values of 0.70 and –0.81 and τ values of 0.51 and –0.51 (Fig. 3 *A*–*C*). We therefore use our extended $\Delta T_s \cdot \Delta t_n$ versus $\Delta T_n \cdot \Delta t_n$ diagram based on the Iberian Margin RI-OH′ record to derive a climatic index, providing values for each DO-AIM pair (Fig. 3*D* and *Materials and Methods*).

We propose a Bipolar Seesaw Index (BSI) to complement the $\Delta T_s \cdot \Delta t_n$ versus $\Delta T_n \cdot \Delta t_n$ diagram (Fig. 3 *C* and *D*). Our BSI is defined for each DO-AIM pair as being the distance along the regression line from the origin (arrows on Fig. 3 *C* and *D*; see exact definition in *Materials and Methods*). Therefore, the BSI depends on both the northern climate event and its southern response. While we could also derive the BSI from the classical ΔT_s versus Δt_n diagram—or the extended ΔT_s versus $\Delta T_n \cdot \Delta t_n$ diagram—based on core MD95-2042 to differentiate H and H-like stadials from other DO stadials, the resulting BSI values would simply mirror Δt_n values expressed in y—or $\Delta T_n \cdot \Delta t_n$ values expressed in normalized °C.y. In addition, BSI values from the classical ΔT_s versus Δt_n diagram based on Greenland ice cores would suggest a single stadial climate state.

As shown in Fig. 3*D* for our Iberian Margin RI-OH′ and Antarctic $\delta^{18}O_{ice}$ stack records, BSI values vary between 841 and 8,023 for H stadials, between 411 and 7,679 for H-like stadials, and between 178 and 859 for other DO stadials. The BSI clearly differentiates H and H-like stadials, including HQ (12, 65) and H5′ (66), from other DO stadials. However, ranges in BSI values overlap for DO stadials with H stadials and DO stadials with H-like stadials, so the BSI cannot fully predict the presence or absence of an IRD layer in core MD95-2042 sediments. H6 has the largest BSI value (8,023), followed by H8 (7,679) and H1 (7,373; Fig. 3*D*). While H8 is an H-like stadial rather than an H stadial off the southern Iberian Margin, given the absence of an IRD layer (58), it has one of the most pronounced peaks in magnetic specific susceptibility as an IRD indicator in core MD95-2042 (67, 68). H8 is also characterized by very low biomarker concentrations in core MD95-2042 (23, 61), likely due to the cessation of seasonal upwelling, as is the case for other H and H-like stadials (61). Furthermore, H8 is linked to one of the most prominent Southern Hemisphere responses (AIM21). By contrast, H2a (841) and H5′ (411) are the only H and H-like stadials with smaller BSI values than DO10, which is the normal DO stadial with the largest BSI value (859; Fig. 3*D*). This overlap may be linked to the short durations of these H-like events and the small warming amplitudes of the associated AIM events. When considering uncertainties in BSI values, as well as the site and proxy dependencies of BSI values, our BSI may further support the existence of at least three climate states during the glacial (64) or even a continuum of thermal bipolar seesaw responses.

Conclusions

Our complementary approaches based on the ΔT_s versus $\Delta T_n \cdot \Delta t_n$ and $\Delta T_s \cdot \Delta t_n$ versus $\Delta T_n \cdot \Delta t_n$ diagrams and associated BSI, together with the comparison between observed and synthetic Antarctic records simulated with the thermal bipolar seesaw model, favor Iberian Margin SST records over Greenland temperature records for discriminating between responses linked to the thermal bipolar seesaw. This is a consequence of H and H-like stadials being severely truncated in Greenland (13, 25) (Fig. 2*A*) but not off the Iberian Margin (23, 27, 56, 57, 61, 62, 69) (Fig. 2 *B* and *C*). The extended sea ice cover and southward shift of AMOC convection

zones likely isolated Greenland, but not the Iberian Margin, from North Atlantic coolings (36–39, 70).

Our data-model comparison clearly shows the importance of the North Atlantic conditions in defining the Southern Ocean response. The fact that the amplitude of the southern response is also correlated to the northern cooling during H and H-like stadials (Fig. 3) implies that the climate system is more complex than a simple flip-flop between two constant states when a threshold is exceeded, suggesting multiple glacial modes or even a continuous response scaled to the forcing during H stadials. North Atlantic SST records should thus be considered in parallel with high-resolution glaciological records, in order to study the tipping points linked to AMOC in the ocean–atmosphere–ice system (71, 72). Indeed, the RI-OH′ and $U^{K'}_{37}$ paleothermometers complement each other for high-resolution SST reconstructions off the southern Iberian Margin. Our work suggests a richer dynamic than was previously thought, which has direct implications for our understanding of past and future climate changes associated with the AMOC and the thermal bipolar seesaw.

Materials and Methods

Biomarker Analysis in Core MD95-2042. We took one sediment sample every 5 cm from core MD95-2042, resulting in an average temporal resolution of roughly 250 y and 638 sediment samples for the last 160 ky. Alkenones and tetraethers were analyzed as described in ref. 23 and references therein. Importantly, the tetraether and alkenone fractions were purified from the same lipid extracts. To strengthen the reliability of tetraether quantifications despite drops in biomarker concentration during cold climatic events and Marine Isotope Stage 1 (27, 61), we doubled the injection volume for the duplicate analyses of the corresponding MD95-2042 samples not previously analyzed when compared to ref. 23.

We selected the homogenized core catcher sample from core MD95-2042 as an in-house standard sediment to verify the absence of instrumental drift, as per ref. 23. Throughout the new sample analyses, we conducted 20 additional replicate analyses of the same standard. We obtained the following SDs from these 20 replicates: 0.007 (0.37 °C) for RI-OH (Ring Index of hydroxylated tetraethers without OH-GDGT-0; introduced by ref. 73), 0.006 (0.14 °C) for RI-OH′ (Ring Index of hydroxylated tetraethers with OH-GDGT-0; introduced by ref. 73), and 0.004 (0.21 °C) for TEX_{86} (TetraEther indeX of GDGTs with 86 carbons; introduced by ref. 74). These SDs are similar to those previously obtained by ref. 23 and are much smaller than the proxy value changes during H and DO stadials (Fig. 2*B* and *SI Appendix*, Fig. S2 *B* and *C*).

Antarctic $\delta^{18}O_{ice}$ and T_{air} Stacks. Given the contrasting AIM shapes between Antarctic $\delta^{18}O_{ice}$ records (49, 70, 75), we used an Antarctic $\delta^{18}O_{ice}$ stack record rather than individual Antarctic $\delta^{18}O_{ice}$ records as the Southern Hemisphere reference record (Fig. 2*D*). To build the Antarctic $\delta^{18}O_{ice}$ stack record, we resampled every 10 y and then centered to zero means and normalized to unit SDs $\delta^{18}O_{ice}$ records from EDC (28, 29), EDML (28, 30), and WD (31–33) over the 140 to 0 ka BP period (see locations in Fig. 1)–the $\delta^{18}O_{ice}$ record from WD, which covers a shorter period than $\delta^{18}O_{ice}$ records from EDC and EDML, was centered to a zero mean and normalized to a unit SD over the 68 to 0 ka BP period. To optimize the continuity between the portions with and without the WD ice core, we shifted Antarctic $\delta^{18}O_{ice}$ records again so that they have zero means over the 68 to 67 ka BP period–the bottom of the WD ice core–before averaging them. We then obtained stacking uncertainties by calculating the pooled SD of the stacked Antarctic $\delta^{18}O_{ice}$ records divided by the square root of the number of stacked Antarctic $\delta^{18}O_{ice}$ records, following ref. 76. To obtain the record plotted in Fig. 2*D* with its 2σ confidence interval (CI), we rescaled the stack with the SD of the $\delta^{18}O_{ice}$ record from EDML over the 140 to 0 ka BP period, expressed in ‰ and then shifted the stack so that its mean value over the 1 to 0 ka BP period is 0. Even if $\delta^{18}O_{ice}$ records reflect not only T_{air} but also the moisture source, the $\delta^{18}O$ of seawater, seasonality, and ice-sheet elevation changes among other factors, $\delta^{18}O_{ice}$ and T_{air} have an almost linear relationship in Antarctica (28, 77–80). In addition, single and dual isotope approaches generally produce similar Antarctic T_{air} records (28, 77, 81). We can thus use the Antarctic $\delta^{18}O_{ice}$ stack record as a proxy for Antarctic T_{air} changes.

We also built an Antarctic T_{air} stack of the EDC, EDML, and WD sites, which requires a correction of $\delta^{18}O_{ice}$ for seawater $\delta^{18}O$ variations due to land ice volume variations. We corrected the EDC, EDML, and WD $\delta^{18}O_{ice}$ records for seawater $\delta^{18}O$ variations following refs. 28 and 76. Before correcting the Antarctic $\delta^{18}O_{ice}$ records, we resampled every 10 y and synchronized the seawater $\delta^{18}O$ record (82)–the record used for ice-volume correction–on the core MD95-2042 benthic foraminiferal $\delta^{18}O$ record (7), itself placed on the core MD95-2042 chronology used in this study (see section *Ice-Core and Core MD95-2042 Chronologies*, below). We then converted the corrected EDC, EDML, and WD $\delta^{18}O_{ice}$ records into T_{air} following ref. 76, before building the Antarctic T_{air} stack as described above.

Ice-Core and Core MD95-2042 Chronologies. The ice-core chronologies for the 60 to 12 ka BP period are based on the latest bipolar synchronization (49) that uses the annual-layer-based Greenland Ice core Chronology 2005 (83–85) modified by ref. 49, with ages multiplied by 1.0063, following ref. 86 for alignment to Chinese speleothems (see locations in Fig. 1; ref. 20)–after 12 ka BP, ice-core records are synchronized on the WAIS Divide ice core chronology 2014 (86, 87) as per ref. 75. The core MD95-2042 chronology for the 43 to 12 ka BP period is obtained using the OxCal 4.4.2 software (88, 89) and previously published ^{14}C ages (68, 90–93) recalibrated with the Marine20 calibration curve (*SI Appendix*, Table S1; ref. 94)–we added two tie points at the core top and at the end of the Younger Dryas to tentatively constrain the core MD95-2042 chronology after 12 ka BP. We corrected ^{14}C ages for a preindustrial marine reservoir age of 500 y ($\Delta R = -50 \pm 100$ y) for consistency with previous studies (91–93), except during H1 ($\Delta R = 350 \pm 200$ y) to take into account the likely larger reservoir age during this H stadial (94–97). While ^{14}C ages older than 41 ky were obtained and gave corresponding calibrated ages older than 43 ky, these ^{14}C ages were deemed imprecise, given their relatively large uncertainties (*SI Appendix*, Table S1). The ice-core chronologies for the 115 to 60 ka BP period and the core MD95-2042 chronology for the 160 to 43 ka BP period were obtained with alignments to Chinese speleothems (20), as described in ref. 23–before 115 ka BP, ice-core records are synchronized on the Antarctic Ice Core Chronology 2012 by refs. 98 and 99. We also adjusted the Antarctic Temperature Stack (76) chronology to the ice-core chronology described here for this study.

Temperature Amplitudes and Event Durations. We named H and H-like stadials as the corresponding H events in ref. 65, except H2 and two H-like stadials. Rather than considering a single H2 stadial, we considered twinned subevents of H2 that we name H2a and H2b after ref. 57, with H2a as a H stadial and H2b as a H-like stadial. We named one H-like stadial H5′ after ref. 27 instead of H5a after ref. 66 and we named C24 the H stadial preceding H10 after ref. 100. We named DO-AIM pairs following the nomenclature of refs. 30, 47, and 48, with DO stadials named after their respective AIM events rather than with the Greenland stadial nomenclature proposed by ref. 101 and adopted by ref. 54.

We calculated ΔT_n and Δt_n values using the T_{air} record from Greenland (25) (Fig. 2*A*) and the $U^{K'}_{37}$ and RI-OH′ SST and ice-volume–corrected planktic foraminiferal $\delta^{18}O$ records from the Iberian Margin core MD95-2042 (Fig. 2 *B* and *C* and *SI Appendix*, Fig. S1*B*; see Fig. 1 for locations and section *Biomarker Analysis in Core MD95-2042* for analytical details, above). We determined ΔT_s values using the Antarctic Temperature Stack (76), the ice-volume–corrected benthic foraminiferal $\delta^{18}O$ record from the Iberian Margin core MD95-2042 (*SI Appendix*, Fig. S1*C*), and our Antarctic $\delta^{18}O_{ice}$ (Fig. 2*D*) and T_{air} stacks (see section *Antarctic* $\delta^{18}O_{ice}$ *and* T_{air} *Stacks*, above). To correct foraminiferal $\delta^{18}O$ records for ice volume changes, we subtracted the seawater $\delta^{18}O$ record (82)–the ice-sheet component–to both foraminiferal $\delta^{18}O$ records after a synchronization on the core MD95-2042 chronology used in this study (see section *Ice-Core and Core MD95-2042 Chronologies*, above) and a resampling of the three $\delta^{18}O$ records every 10 y. Given the opposite correlation between foraminiferal $\delta^{18}O$ and temperature–SST or deep ocean temperature for planktic and benthic foraminifera, respectively–in comparison with the other selected paleothermometric proxies, we took the opposite values of both ice-volume–corrected foraminiferal $\delta^{18}O$ records before calculating their Δt_n, ΔT_n, and ΔT_s values. We also calculated ΔT_n and Δt_n values using band-pass–filtered Northern Hemisphere records and ΔT_s values using band-pass–filtered or simulated Southern Hemisphere records (see section *Thermal Bipolar Seesaw Model*, below).

To determine ΔT_s values, we took the difference between the value at the onset of the AIM event and the highest AIM value (*SI Appendix*, Fig. S14 *D* and *H*).

We calculated ΔT_n values following two end-member scenarios (*SI Appendix*, Fig. S14 *A–C* and *E–G* and Text S8). For Scenario 1, we defined ΔT_n values as the difference between the lowest DO stadial value and the value at the start of the abrupt transition to the DO stadial. As was recently performed by ref. 54, we determined visually the start of the abrupt transition to the DO stadial. For Scenario 2, we defined ΔT_n values as the difference between the lowest DO stadial value and the highest preceding DO interstadial value. We obtained a set of ΔT_n and ΔT_s values for each of the observed, filtered, and simulated temperature records that we selected. For observed ice-core records, we generated a 5-point moving average for NGRIP T_{air} and 11-point moving averages for Antarctic stacks in order to suppress the influence of high-frequency noise.

To determine Δt_n values, we determined visually the midpoints of DO stadial onsets and terminations, as was recently performed by ref. 54 (*SI Appendix*, Fig. S14 *A–C* and *E–G*). We obtained a set of Δt_n values for Greenland and another set of Δt_n values for the Iberian Margin. We first applied a 5-point moving average for NGRIP T_{air} in order to facilitate Δt_n value determination.

To allow the relative comparison of temperature amplitudes between Greenland and the Iberian Margin (*SI Appendix*, Text S5) and to circumvent the imperfections of existing proxy-temperature calibrations (25, 27, 59, 60, 73, 102–106), we centered to zero means and normalized to unit SDs all observed Northern and Southern Hemisphere temperature records over the 129 to 0 ka BP period, which is covered by all paleothermometric records plotted in Fig. 2 *A–D* and *SI Appendix*, Fig. S1. Consequently, $\Delta T_n{\cdot}\Delta t_n$ and $\Delta T_s{\cdot}\Delta t_n$ values are expressed in normalized °C.y rather than in °C.y.

We excluded a few problematic DO-AIM pairs occurring during the last 160 ky from our analysis. Indeed, the DO stadials paired with AIM23, AIM21, and AIM14 have submillennial warm events in Greenland (Fig. 2*A* and *SI Appendix*, Fig. S14 *A* and *E*) which are poorly resolved, if at all, in the Iberian Margin (Fig. 2 *B* and *C* and *SI Appendix*, Fig. S14 *B*, *C*, *F*, and *G*). We thus treated DO stadials 23, 21, and 14–equivalent to Greenland stadials GS24, GS22, and GS15 in ref. 23–as single events for all Northern Hemisphere records. Following ref. 54, we excluded two DO stadials shorter than 300 y–named Greenland stadials GS17.2 and GS16.2 in ref. 54–and their Southern Hemisphere counterparts from our study. The DO stadials paired with AIM16 and AIM15 thus correspond to Greenland stadials GS17.1 and GS16.1 in ref. 54, respectively. Given their very small AIM amplitudes and very short DO stadial durations (Fig. 2 *A* and *D*), we excluded the DO-AIM pairs 22 and 13. Given their lower resolution compared with Greenland paleothermometric records, the Iberian Margin SST records did not allow to simulate the DO-AIM pair 9 (Fig. 4). Therefore, we excluded the DO-AIM pair 9 from all Southern versus Northern Hemisphere diagrams based on synthetic Southern Hemisphere records simulated with the Iberian Margin SST records.

Bipolar Seesaw Index. We defined the Bipolar Seesaw Index (BSI) as the distance between the origin and the orthogonal projection on the regression line of each point in the $\Delta T_s{\cdot}\Delta t_n$ versus $\Delta T_n{\cdot}\Delta t_n$ diagram (Eq. **2**). As a representative example, we provide the BSI for the $\Delta T_s{\cdot}\Delta t_n$ versus $\Delta T_n{\cdot}\Delta t_n$ diagram for our Antarctic $\delta^{18}O_{ice}$ stack and our core MD95-2042 RI-OH′ record (Fig. 3 *C* and *D*). We first determined the slope (S) of the regression line through the origin of all points by using the "deming" function of the deming R package (107). For simplicity we took similar errors on both coordinates for all points: 1 y for Δt_n values, 0.001 (normalized) °C for ΔT_s values, and 1 (normalized) °C.y for $\Delta T_n{\cdot}\Delta t_n$ and $\Delta T_s{\cdot}\Delta t_n$ values. We then calculated the BSI as the distance between the origin and the orthogonal projection:

$$\mathrm{BSI} = \frac{\left|\Delta T_n \cdot \Delta t_n + S{\cdot}\Delta T_s{\cdot}\Delta t_n\right|}{\sqrt{1+S^2}}. \qquad [2]$$

Thermal Bipolar Seesaw Model. To generate synthetic Southern Hemisphere signals (T_S) from Northern Hemisphere signals (T_N) convoluted with the time characteristic of the heat reservoir (T = 1,120 y, as per ref. 46), we solved the differential equation Eq. **3** (Equation 1 in ref. 46) every 10 y using the "ode" function of the "deSolve" R package (108):

$$\frac{dT_S(t)}{dt} = \frac{1}{\mathrm{T}}\left[-T_N(t) - T_S(t)\right]. \qquad [3]$$

To focus on the abrupt variability, we centered to zero means the evenly resampled records (every 10 y) before applying a fourth-order Butterworth band-pass filter (500- to 10,000-y or 500- to 16,000-y window) over the 7 to 120 or 4 to 123 ka BP period to limit the edge effect over the 12 to 115 ka BP period. We used the "linterp" function of the "astrochron" R package (109) for resampling and the "butterworth.wge" function of the "tsgwe" R package (110, 111) for filtering. We then used the "ccf" R function (112) for phase relationship analyses. We assumed that the first $T_S(k_0)$ value at 120 or 123 ka BP is 0, following refs. 46 and 113–see *SI Appendix*, Text S10 for comparisons with a discretized thermal bipolar seesaw model and considerations about the T value.

Uncertainty Analysis. We employed a Monte Carlo method modified from ref. 54. Using the "MonteCarlo" R package (114), we randomly perturbed all Northern and Southern Hemisphere temperature records by drawing all their data points from normal distributions centered on their measured values and with SDs set as the analytical uncertainties for the core MD95-2042 RI-OH′ (0.008 RI-OH′ units equivalent to 0.19 °C based on 37 replicate analyses of the same standard; this study), $U^{K'}_{37}$ (0.010 $U^{K'}_{37}$ units equivalent to 0.26 °C; ref. 27), and planktic and benthic foraminiferal $\delta^{18}O$ values (0.1‰; ref. 69), the 1σ CIs around our Antarctic $\delta^{18}O_{ice}$ and T_{air} stacks, and the rms errors between raw and 500-y smoothed time series–with a fourth-order Butterworth low-pass filter–for NGRIP T_{air} (0.85 °C) and $\delta^{18}O_{ice}$ (0.60‰). For simplicity, we used the same delimitations for event durations and temperature amplitudes as those based on original temperature records for all Monte Carlo iterations. For comparison purposes, we also randomly perturbed ΔT_n values for Greenland by drawing them from normal distributions centered on the calculated ΔT_n values and with SDs set as the published uncertainty in ΔT_n values (1σ = 1.5 °C; ref. 25). After 1,000 Monte Carlo iterations, we repeated all analyses for each iteration–except the interhemispheric correlations for restricted populations of DO-AIM pairs, given the typically nonsignificant correlations–and reported 95% CIs as intervals between the 2.5th and 97.5th percentiles.

We also employed a bootstrapping method as a complement to the Monte Carlo method in order to compare interhemispheric correlations as depicted by Southern versus Northern Hemisphere diagrams. Using the "boot" R package (115, 116), we ran 1,000 bootstrap iterations for each correlation comparison and reported 95% CIs of the differences in absolute coefficient correlation values. Here again, we focused on interhemispheric correlations for all DO-AIM pairs.

Data, Materials, and Software Availability. All new data are available at Zenodo and PANGAEA: https://doi.org/10.5281/zenodo.7587300 (117). Previously published tetraether-based data from core MD95-2042 for the 160 to 45 ka BP period are available at https://doi.pangaea.de/10.1594/PANGAEA.927622. Alkenone-based data from core MD95-2042 are available in the supplement of ref. 27 for the 70 to 0 ka BP period and at https://doi.pangaea.de/10.1594/PANGAEA.927622 for the 160 to 70 ka BP period. Foraminiferal $\delta^{18}O$ data from core MD95-2042 are available at https://doi.pangaea.de/10.1594/PANGAEA.60829 and https://doi.pangaea.de/10.1594/PANGAEA.58195 for planktic foraminiferal $\delta^{18}O$ and at https://doi.pangaea.de/10.1594/PANGAEA.58228 for benthic foraminiferal $\delta^{18}O$. T_{air} reconstructions from Greenland are available in the supplements of refs. 24, 25, and 26, at https://www.ncdc.noaa.gov/paleo/study/22057 and https://www.ncdc.noaa.gov/paleo/study/24371 for GISP2 and NGRIP, respectively, and at https://doi.pangaea.de/10.1594/PANGAEA.905451 for GISP2. $\delta^{18}O_{ice}$ data from the NGRIP are available at https://www.iceandclimate.nbi.ku.dk/data/2010-11-19_GICC05modelext_for_NGRIP.txt and https://doi.pangaea.de/10.1594/PANGAEA.824889. $\delta^{18}O_{ice}$ data from Antarctica are available at https://www.ncdc.noaa.gov/paleo/study/27950 for EDC, at https://www.ncdc.noaa.gov/paleo/study/27950 and https://doi.pangaea.de/10.1594/PANGAEA.824888 for EDML, and in the supplement of ref. 31 for WD. Seawater $\delta^{18}O$ data are available at https://www.ncdc.noaa.gov/paleo/study/11933. The Antarctic Temperature Stack is available in the supplement of ref. 76 and at https://doi.pangaea.de/10.1594/PANGAEA.810188. The Southern Ocean SST records and stack plotted in *SI Appendix*, Fig. S6 *A–C* are available at https://doi.pangaea.de/10.1594/PANGAEA.931020, https://doi.pangaea.de/10.1594/PANGAEA.931025, and https://doi.pangaea.de/10.1594/PANGAEA.912158.

ACKNOWLEDGMENTS. Coring of MD95-2042 by the R/V Marion Dufresne was supported by the International Marine Global Change Study program. Work at CEREGE is supported by the Collège de France, including a postdoctoral salary

for N.D. We thank the referees for their numerous constructive comments: T. Stocker notably for pointing to his course for a better physical motivation of our approach and for suggesting to model idealized records; J. McManus in particular for asking for more justification on paleothermometric proxies and discussion on the chronological uncertainties; and E. Rohling notably for requesting the consideration of southern SSTs and quantitative assessments of uncertainties and of the slope of the North-South correlations in relation to heat exchange.

Author affiliations: [a]CEREGE, Aix-Marseille University, CNRS, IRD, INRAE, Collège de France, Technopôle de l'Arbois, 13545 Aix-en-Provence, France

1. D. A. Smeed *et al.*, Observed decline of the Atlantic meridional overturning circulation 2004–2012. *Ocean Sci.* **10**, 29–38 (2014).
2. L. Caesar, S. Rahmstorf, A. Robinson, G. Feulner, V. Saba, Observed fingerprint of a weakening Atlantic Ocean overturning circulation. *Nature* **556**, 191–196 (2018).
3. M. Dima, G. Lohmann, Evidence for two distinct modes of large-scale ocean circulation changes over the last century. *J. Clim.* **23**, 5–16 (2010).
4. W. Weijer, W. Cheng, O. A. Garuba, A. Hu, B. T. Nadiga, CMIP6 models predict significant 21st century decline of the Atlantic Meridional Overturning Circulation. *Geophys. Res. Lett.* **47**, e2019GL086075 (2020).
5. K. H. Kilbourne *et al.*, Atlantic circulation change still uncertain. *Nat. Geosci.* **15**, 165–167 (2022).
6. T. F. Stocker, A. Schmittner, Influence of CO_2 emission rates on the stability of the thermohaline circulation. *Nature* **388**, 862–865 (1997).
7. N. J. Shackleton, M. A. Hall, E. Vincent, Phase relationships between millennial-scale events 64000–24000 years ago. *Paleoceanography* **15**, 565–569 (2000).
8. J. F. McManus, R. Francois, J.-M. Gherardi, L. D. Keigwin, S. Brown-Leger, Collapse and rapid resumption of Atlantic meridional circulation linked to deglacial climate changes. *Nature* **428**, 834–837 (2004).
9. A. M. Piotrowski, S. L. Goldstein, S. R. Hemming, R. G. Fairbanks, Temporal relationships of carbon cycling and ocean circulation at glacial boundaries. *Science* **307**, 1933–1938 (2005).
10. L. G. Henry *et al.*, North Atlantic ocean circulation and abrupt climate change during the last glaciation. *Science* **353**, 470–474 (2016).
11. H. C. Ng *et al.*, Coherent deglacial changes in western Atlantic Ocean circulation. *Nat. Commun.* **9**, 2947 (2018).
12. Y. Zhou *et al.*, Enhanced iceberg discharge in the western North Atlantic during all Heinrich events of the last glaciation. *Earth Planet. Sci. Lett.* **564**, 116910. (2021).
13. North Greenland Ice Core Project members, High-resolution record of Northern Hemisphere climate extending into the last interglacial period. *Nature* **431**, 147–151 (2004).
14. G. C. Bond *et al.*, Correlations between climate records from North Atlantic sediments and Greenland ice. *Nature* **365**, 143–147 (1993).
15. W. Dansgaard *et al.*, Evidence for general instability of past climate from a 250-kyr ice-core record. *Nature* **364**, 218–220 (1993).
16. W. Dansgaard *et al.*, "North Atlantic climatic oscillations revealed by deep Greenland ice cores" in *Climate Processes and Climate Sensitivity*, (American Geophysical Union AGU, 1984), pp. 288–298.
17. H. Oeschger *et al.*, "Late glacial climate history from ice cores" in *Climate Processes and Climate Sensitivity*, (American Geophysical Union AGU, 1984), pp. 299–306.
18. H. Heinrich, Origin and consequences of cyclic ice rafting in the Northeast Atlantic Ocean during the past 130,000 years. *Q. Res.* **29**, 142–152 (1988).
19. J. B. Pedro *et al.*, Dansgaard-Oeschger and Heinrich event temperature anomalies in the North Atlantic set by sea ice, frontal position and thermocline structure. *Q. Sci. Rev.* **289**, 107599 (2022).
20. H. Cheng *et al.*, The Asian monsoon over the past 640,000 years and ice age terminations. *Nature* **534**, 640–646 (2016).
21. K. S. Casey, T. B. Brandon, P. Cornillon, R. Evans, "The past, present, and future of the AVHRR pathfinder SST program" in *Oceanography from Space: Revisited*, V. Barale, J. F. R. Gower, L. Alberotanza, Eds. (Springer, Netherlands, 2010), pp. 273–287.
22. K. S. Casey, E. J. Kearns, V. Halliwell, R. Evans, AVHRR Pathfinder version 5.0 and 5.1 global 4km sea surface temperature (SST) daily, 5-day, and monthly harmonic climatologies for 1982-2008. [monthly]. NOAA National Centers for Environmental Information. Dataset (2011). https://www.ncei.noaa.gov/archive/accession/AVHRR_Pathfinder-NODC-v5.0_v5.1-climatologies (Accessed 15 January 2020).
23. N. Davtian, E. Bard, S. Darfeuil, G. Ménot, F. Rostek, The novel hydroxylated tetraether index RI-OH′ as a sea surface temperature proxy for the 160–45 ka BP period off the Iberian Margin. *Paleoceanogra. Paleoclimatol.* **36**, e2020PA004077 (2021).
24. T. Kobashi *et al.*, Volcanic influence on centennial to millennial Holocene Greenland temperature change. *Sci. Rep.* **7**, 1441 (2017).
25. P. Kindler *et al.*, Temperature reconstruction from 10 to 120 kyr b2k from the NGRIP ice core. *Clim. Past* **10**, 887–902 (2014).
26. NEEM community members, Eemian interglacial reconstructed from a Greenland folded ice core. *Nature* **493**, 489–494 (2013).
27. S. Darfeuil *et al.*, Sea surface temperature reconstructions over the last 70 kyr off Portugal: Biomarker data and regional modeling. *Paleoceanography* **31**, 40–65 (2016).
28. B. Stenni *et al.*, The deuterium excess records of EPICA Dome C and Dronning Maud Land ice cores (East Antarctica). *Q. Sci. Rev.* **29**, 146–159 (2010).
29. EPICA community members, Eight glacial cycles from an Antarctic ice core. *Nature* **429**, 623–628 (2004).
30. EPICA Community Members, One-to-one coupling of glacial climate variability in Greenland and Antarctica. *Nature* **444**, 195–198 (2006).
31. WAIS Divide Project Members, Precise interpolar phasing of abrupt climate change during the last ice age. *Nature* **520**, 661–665 (2015).
32. E. J. Steig *et al.*, Recent climate and ice-sheet changes in West Antarctica compared with the past 2,000 years. *Nat. Geosci.* **6**, 372–375 (2013).
33. WAIS Divide Project Members, Onset of deglacial warming in West Antarctica driven by local orbital forcing. *Nature* **500**, 440–444 (2013).
34. S. J. Johnsen *et al.*, Irregular glacial interstadials recorded in a new Greenland ice core. *Nature* **359**, 311–313 (1992).
35. P. M. Grootes, M. Stuiver, J. W. C. White, S. Johnsen, J. Jouzel, Comparison of oxygen isotope records from the GISP2 and GRIP Greenland ice cores. *Nature* **366**, 552–554 (1993).
36. A. Ganopolski, S. Rahmstorf, Rapid changes of glacial climate simulated in a coupled climate model. *Nature* **409**, 153–158 (2001).
37. C. Li, D. S. Battisti, D. P. Schrag, E. Tziperman, Abrupt climate shifts in Greenland due to displacements of the sea ice edge. *Geophys. Res. Lett.* **32**, L19702 (2005).
38. C. Li, D. S. Battisti, C. M. Bitz, Can North Atlantic sea ice anomalies account for Dansgaard-Oeschger climate signals? *J. Clim.* **23**, 5457–5475 (2010).
39. C. Li, A. Born, Coupled atmosphere-ice-ocean dynamics in Dansgaard-Oeschger events. *Q. Sci. Rev.* **203**, 1–20 (2019).
40. C. He *et al.*, Abrupt Heinrich Stadial 1 cooling missing in Greenland oxygen isotopes. *Sci. Adv.* **7**, eabh1007 (2021).
41. R. Knutti, J. Flückiger, T. F. Stocker, A. Timmermann, Strong hemispheric coupling of glacial climate through freshwater discharge and ocean circulation. *Nature* **430**, 851–856 (2004).
42. R. J. Stouffer *et al.*, Investigating the causes of the response of the thermohaline circulation to past and future climate changes. *J. Clim.* **19**, 1365–1387 (2006).
43. Z. Liu *et al.*, Transient simulation of last deglaciation with a new mechanism for Bølling-Allerød warming. *Science* **325**, 310–314 (2009).
44. J. B. Pedro *et al.*, Beyond the bipolar seesaw: Toward a process understanding of interhemispheric coupling. *Q. Sci. Rev.* **192**, 27–46 (2018).
45. T. F. Stocker, The seesaw effect. *Science* **282**, 61–62 (1998).
46. T. F. Stocker, S. J. Johnsen, A minimum thermodynamic model for the bipolar seesaw. *Paleoceanography* **18**, 1087 (2003).
47. E. Capron *et al.*, Synchronising EDML and NorthGRIP ice cores using $\delta^{18}O$ of atmospheric oxygen ($\delta^{18}O_{atm}$) and CH_4 measurements over MIS 5 (80–123 kyr). *Q. Sci. Rev.* **29**, 222–234 (2010).
48. E. Capron *et al.*, Millennial and sub-millennial scale climatic variations recorded in polar ice cores over the last glacial period. *Clim. Past* **6**, 345–365 (2010).
49. A. Svensson *et al.*, Bipolar volcanic synchronization of abrupt climate change in Greenland and Antarctic ice cores during the last glacial period. *Clim. Past* **16**, 1565–1580 (2020).
50. T. Blunier, E. J. Brook, Timing of millennial-scale climate change in Antarctica and Greenland during the last glacial period. *Science* **291**, 109–112 (2001).
51. B. Stenni *et al.*, Expression of the bipolar see-saw in Antarctic climate records during the last deglaciation. *Nat. Geosci* **4**, 46–49 (2011).
52. M. Siddall *et al.*, Using a maximum simplicity paleoclimate model to simulate millennial variability during the last four glacial periods. *Q. Sci. Rev.* **25**, 3185–3197 (2006).
53. V. Margari *et al.*, The nature of millennial-scale climate variability during the past two glacial periods. *Nat. Geosci.* **3**, 127–131 (2010).
54. P. Zheng, J. B. Pedro, M. Jochum, S. O. Rasmussen, Z. Lai, Different trends in Antarctic temperature and atmospheric CO_2 during the last glacial. *Geophys. Res. Lett.* **48**, e2021GL093868 (2021).
55. P. J. Reimer *et al.*, The IntCal20 Northern Hemisphere radiocarbon age calibration curve (0–55 cal kBP). *Radiocarbon* **62**, 725–757 (2020).
56. E. Bard *et al.*, Retreat velocity of the North Atlantic polar front during the last deglaciation determined by ^{14}C accelerator mass spectrometry. *Nature* **328**, 791–794 (1987).
57. E. Bard, F. Rostek, J.-L. Turon, S. Gendreau, Hydrological impact of Heinrich events in the subtropical northeast Atlantic. *Science* **289**, 1321–1324 (2000).
58. F. Eynaud, J. L. Turon, M. F. Sánchez-Goñi, S. Gendreau, Dinoflagellate cyst evidence of 'Heinrich-like events' off Portugal during the Marine Isotopic Stage 5. *Marine Micropaleontol.* **40**, 9–21 (2000).
59. C. Buizert *et al.*, Antarctic surface temperature and elevation during the Last Glacial Maximum. *Science* **372**, 1097–1101 (2021).
60. B. R. Markle, E. J. Steig, Improving temperature reconstructions from ice-core water-isotope records. *Clim. Past* **18**, 1321–1368 (2022).
61. D. Pailler, E. Bard, High frequency palaeoceanographic changes during the past 140 000 yr recorded by the organic matter in sediments of the Iberian Margin. *Palaeogeogra. Palaeoclimatol. Palaeoecol.* **181**, 431–452 (2002).
62. B. Martrat *et al.*, Four climate cycles of recurring deep and surface water destabilizations on the Iberian Margin. *Science* **317**, 502–507 (2007).
63. T. F. Stocker, *Introduction to Climate Modelling* (University of Bern, 2022), pp. 1–209, https://climatehomes.unibe.ch/~stocker/stocker22icm.pdf.
64. R. B. Alley, P. U. Clark, The deglaciation of the Northern Hemisphere: A global perspective. *Annu. Rev. Earth Planet. Sci.* **27**, 149–182 (1999).
65. J. N. Bassis, S. V. Petersen, L. Mac Cathles, Heinrich events triggered by ocean forcing and modulated by isostatic adjustment. *Nature* **542**, 332–334 (2017).
66. H. Rashid, R. Hesse, D. J. W. Piper, Evidence for an additional Heinrich event between H5 and H6 in the Labrador Sea. *Paleoceanography* **18**, 1077 (2003).
67. N. Thouveny *et al.*, Rock magnetic detection of distal ice-rafted debries: Clue for the identification of Heinrich layers on the Portuguese margin. *Earth Planet. Sci. Lett.* **180**, 61–75 (2000).
68. E. Bard, F. Rostek, G. Ménot-Combes, Radiocarbon calibration beyond 20,000 ^{14}C yr B.P. by means of planktonic foraminifera of the Iberian Margin. *Q. Res.* **61**, 204–214 (2004).
69. O. Cayre, Y. Lancelot, E. Vincent, M. A. Hall, Paleoceanographic reconstructions from planktonic foraminifera off the Iberian Margin: Temperature, salinity, and Heinrich events. *Paleoceanography* **14**, 384–396 (1999).
70. A. Landais *et al.*, A review of the bipolar see–saw from synchronized and high resolution ice core water stable isotope records from Greenland and East Antarctica. *Q. Sci. Rev.* **114**, 18–32 (2015).
71. A. A. Cimatoribus, S. S. Drijfhout, V. Livina, G. van der Schrier, Dansgaard-Oeschger events: Bifurcation points in the climate system. *Clim. Past* **9**, 323–333 (2013).
72. V. Brovkin *et al.*, Past abrupt changes, tipping points and cascading impacts in the Earth system. *Nat. Geosci.* **14**, 550–558 (2021).

73. X. Lü *et al.*, Hydroxylated isoprenoid GDGTs in Chinese coastal seas and their potential as a paleotemperature proxy for mid-to-low latitude marginal seas. *Org. Geochem.* **89–90**, 31–43 (2015).
74. S. Schouten, E. C. Hopmans, E. Schefuß, J. S. Sinninghe Damsté, Distributional variations in marine crenarchaeotal membrane lipids: A new tool for reconstructing ancient sea water temperatures? *Earth Planet. Sci. Lett.* **204**, 265–274 (2002).
75. C. Buizert *et al.*, Abrupt ice-age shifts in southern westerly winds and Antarctic climate forced from the north. *Nature* **563**, 681–685 (2018).
76. F. Parrenin *et al.*, Synchronous change of atmospheric CO_2 and Antarctic temperature during the last deglacial warming. *Science* **339**, 1060–1063 (2013).
77. J. Jouzel *et al.*, Orbital and millennial Antarctic climate variability over the past 800,000 years. *Science* **317**, 793–796 (2007).
78. G. Delaygue, J. Jouzel, V. Masson, R. D. Koster, E. Bard, Validity of the isotopic thermometer in central Antarctica: Limited impact of glacial precipitation seasonality and moisture origin. *Geophys. Res. Lett.* **27**, 2677–2680 (2000).
79. J. Jouzel *et al.*, Magnitude of isotope/temperature scaling for interpretation of central Antarctic ice cores. *J. Geophys. Res. Atmosp.* **108**, 4361 (2003).
80. M. Werner, J. Jouzel, V. Masson-Delmotte, G. Lohmann, Reconciling glacial Antarctic water stable isotopes with ice sheet topography and the isotopic paleothermometer. *Nat. Commun.* **9**, 3537 (2018).
81. B. Stenni *et al.*, A late-glacial high-resolution site and source temperature record derived from the EPICA Dome C isotope records (East Antarctica). *Earth Planet. Sci. Lett.* **217**, 183–195 (2004).
82. R. Bintanja, R. S. W. van de Wal, North American ice-sheet dynamics and the onset of 100,000-year glacial cycles. *Nature* **454**, 869–872 (2008).
83. K. K. Andersen *et al.*, The Greenland Ice core chronology 2005, 15–42 ka. Part 1: Constructing the time scale. *Q. Sci. Rev.* **25**, 3246–3257 (2006).
84. A. Svensson *et al.*, A 60 000 year Greenland stratigraphic ice core chronology. *Clim. Past* **4**, 47–57 (2008).
85. S. O. Rasmussen *et al.*, A new Greenland ice core chronology for the last glacial termination. *J. Geophys. Res. Atmosp.* **111**, D06102 (2006).
86. C. Buizert *et al.*, The WAIS Divide deep ice core WD2014 chronology–Part 1: Methane synchronization (68–31 ka BP) and the gas age–ice age difference. *Clim. Past* **11**, 153–173 (2015).
87. M. Sigl *et al.*, The WAIS divide deep ice core WD2014 chronology–Part 2: Annual-layer counting (0–31 ka BP). *Clim. Past* **12**, 769–786 (2016).
88. C. Bronk Ramsey, Bayesian analysis of radiocarbon dates. *Radiocarbon* **51**, 337–360 (2009).
89. C. Bronk Ramsey, OxCal 4.4.2. https://c14.arch.ox.ac.uk/oxcal.html (Accessed 11 September 2020).
90. E. Bard, F. Rostek, G. Ménot-Combes, A better radiocarbon clock. *Science* **303**, 178–179 (2004).
91. E. Bard, G. Ménot-Combes, F. Rostek, Present status of radiocarbon calibration and comparison records based on Polynesian corals and Iberian margin sediments. *Radiocarbon* **46**, 1189–1202 (2004).
92. N. J. Shackleton, R. G. Fairbanks, T. Chiu, F. Parrenin, Absolute calibration of the Greenland time scale: implications for Antarctic time scales and for $\Delta^{14}C$. *Q. Sci. Rev.* **23**, 1513–1522 (2004).
93. E. Bard *et al.*, Radiocarbon calibration/comparison records based on marine sediments from the Pakistan and Iberian Margins. *Radiocarbon* **55**, 1999–2019 (2013).
94. T. J. Heaton *et al.*, Marine20–The marine radiocarbon age calibration curve (0–55,000 cal BP). *Radiocarbon* **62**, 779–820 (2020).
95. J. V. Stern, L. E. Lisiecki, North Atlantic circulation and reservoir age changes over the past 41,000 years. *Geophys. Res. Lett.* **40**, 3693–3697 (2013).
96. C. Waelbroeck *et al.*, The timing of the last deglaciation in North Atlantic climate records. *Nature* **412**, 724–727 (2001).
97. L. C. Skinner *et al.*, Atlantic Ocean ventilation changes across the last deglaciation and their carbon cycle implications. *Paleoceanogra. Paleoclimatol.* **36**, e2020PA004074 (2021).
98. D. Veres *et al.*, The Antarctic ice core chronology (AICC2012): An optimized multi-parameter and multi-site dating approach for the last 120 thousand years. *Clim. Past* **9**, 1733–1748 (2013).
99. L. Bazin *et al.*, An optimized multi-proxy, multi-site Antarctic ice and gas orbital chronology (AICC2012): 120–800 ka. *Clim. Past* **9**, 1715–1731 (2013).
100. J. F. McManus *et al.*, High-resolution climate records from the North Atlantic during the last interglacial. *Nature* **371**, 326–329 (1994).
101. S. O. Rasmussen *et al.*, A stratigraphic framework for abrupt climatic changes during the Last Glacial period based on three synchronized Greenland ice-core records: Refining and extending the INTIMATE event stratigraphy. *Q. Sci. Rev.* **106**, 14–28 (2014).
102. S. Fietz, S. L. Ho, C. Huguet, Archaeal membrane lipid-based paleothermometry for applications in polar oceans. *Oceanog* **33**, 104–114 (2020).
103. J. E. Tierney, M. P. Tingley, A. Bayesian, spatially-varying calibration model for the TEX_{86} proxy. *Geochim. et Cosmochim. Acta* **127**, 83–106 (2014).
104. J. E. Tierney, M. P. Tingley, A TEX_{86} surface sediment database and extended Bayesian calibration. *Sci. Data* **2**, 150029 (2015).
105. M. H. Conte *et al.*, Global temperature calibration of the alkenone unsaturation index ($U^{K'}_{37}$) in surface waters and comparison with surface sediments. *Geochem. Geophys. Geosyst.* **7**, Q02005 (2006).
106. J. E. Tierney, M. P. Tingley, BAYSPLINE: A new calibration for the alkenone paleothermometer. *Paleoceanogra. Paleoclimatol.* **33**, 281–301 (2018).
107. T. Therneau, Deming, Theil-Sen, Passing-Bablock and Total Least Squares Regression (R package version 1.4, 2018).
108. K. Soetaert, T. Petzoldt, R. W. Setzer, Solving differential equations in R: Package deSolve. *J. Stat. Software* **33**, 1–25 (2010).
109. S. R. Meyers, Astrochron: An R package for astrochronology (R package version 1.1, 2021).
110. W. A. Woodward, tswge: Time Series for Data Science (R package version 2.0.0, 2022).
111. W. A. Woodward, H. L. Gray, A. C. Elliott, *Applied Time Series Analysis with R* (CRC Press, ed. 2, 2017).
112. R Core Team, *R: A language and environment for statistical computing* (Version 4.2.2, R Foundation for Statistical Computing, Vienna, Austria, 2022)
113. T. F. Stocker, S. J. Johnsen, Correction to "A minimum thermodynamic model for the bipolar seesaw". *Paleoceanography* **20**, PA1002 (2005).
114. C. H. Leschinski, MonteCarlo: Automatic Parallelized Monte Carlo Simulations (R package version 1.0.6, 2019).
115. A. Canty, B. Ripley, boot: Bootstrap R (S-Plus) Functions (R package version 1.3-28.1, 2022).
116. A. C. Davidson, D. V. Hinkley, *Bootstrap Methods and Their Applications* (Cambridge University Press, 1997).
117. N. Davtian, E. Bard, Biomarker indices and concentrations and biomarker-based temperature estimates from the Iberian Margin core MD95-2042, composite atmospheric temperature record from Greenland, and stacks of delta 18Oice and atmospheric temperature records from three Antarctic sites. Zenodo. https://doi.org/10.5281/zenodo.7587300 (Deposited 30 January 2023).